RSC Advances

PAPER

View Article Online
View Journal | View Issue

Cite this: *RSC Adv.*, 2022, **12**, 16412

Enhancement of dielectric performance of encapsulation in barium titanate oxide using size-controlled reduced graphene oxide

So-Yeon Jun,[ab] SeungHun Park,[b] Nam Wuk Baek,[b] Tae-Young Lee,[a] Sehoon Yoo,[a] Donggeun Jung[b] and Jin-Young Kim*[c]

Received 25th February 2022
Accepted 23rd May 2022

DOI: 10.1039/d2ra01266a

rsc.li/rsc-advances

Ferroelectric barium titanate (BTO) powder particles were encapsulated by three different sizes of reduced graphene oxide (rGO) platelets. The size of the graphene oxide (GO) platelets is controlled by varying the horn type ultrasonic times, *i.e.* 0, 30, and 60 min, respectively, and they are reduced with hydrazine to obtain rGO-encapsulated BTO (rGO@BTO) film. The rGO@BTO film exhibits an increase in the dielectric characteristics due to the interfacial polarization. These improved characteristics include a dielectric constant of 194 (a large increment of 111%), along with the dielectric loss of 0.053 (a slight increment of 13%) at 1 kHz, compared to the pure BTO dielectric film. The improvement in the dielectric constant of the rGO@BTO is attributed to the encapsulation degree between the rGO platelets and BTO powder particles, which results in the interfacial polarization and micro-capacitor effect in a dielectric film, and also contributes to a low dielectric loss. Therefore, a suitable size of rGO platelets for encapsulation is essential for high-dielectric performance.

Introduction

Nano-composites composed of reduced graphene oxide (rGO) platelets and polymer have gained considerable interest due to their potential applications in various fields, such as super-capacitors,[1] batteries,[2] field effect transistors,[3] membranes,[4,5] biomedicines,[6] and photocatalysts.[7] A common method for the synthesis of graphene-based nano-composites has been reported.[8,9] Currently, rGO platelets are used as conductive materials for dielectric films, owing to their flexibility and high conductivity. However, they present major drawbacks such as dielectric losses (tan δ).[10–12]

The dielectric properties of conductive materials, typically nanometer-sized materials, have been extensively analysed for potential applications such as electric energy storage,[13] electroluminescent devices,[14] gate dielectric,[15] and embedded capacitors.[15] Some similar studies have been reported such as Ni in $BaTiO_3$ of a composition of $(Ba_{0.5}Ni_{0.5})TiO_3$ for the temperature sensor[16] and bandwidth applications and gold nanoparticles incorporated in the reduced graphene oxide for developing filtering and modulating functions in 2D devices.[17] Consequently, two-phase (conductive material/polymer)[18–20] or three-phase composite materials (ferroelectric ceramic powder/conductive material/polymer)[13,21–24] have been analysed extensively. A drastic increase in the dielectric constant has been reported when approaching the percolation threshold of conductive fillers.[25,26] The percolation theory was used to derive the insulator–conductor transition induced at the critical threshold.[27] The two-phase[19,20,28] and three-phase[13,21–24] composite films have been reported to have high dielectric constants, but they present disadvantages such as excessive thickness, complicated fabrication processes, and high sintering temperatures (over 1300 °C).

A method involving the encapsulation of barium titanate (BTO) powder particles in rGO platelets and subsequent mixing, was used to obtain a high dielectric constant and a low dielectric loss.[28] When rGO platelets are encapsulated, the size of graphene also plays a crucial role in the conductivity.[29] The large size of the rGO platelets is a major obstacle due to its percolation in the film. The rGO platelets promote the high dielectric constant due to the metal–insulator-transition (MIT) phase transition with the high dielectric loss through the leakage bypass network.

This paper analyses the dielectric characteristics of polymer composites to achieve a high dielectric constant and low dielectric loss in the dielectric film. Ferroelectric barium titanate (BTO) powder particles are encapsulated by reduced graphene oxide (rGO). The size of the rGO platelets is controlled by the horn type ultra-sonication times of 0, 30, and 60 min, respectively. Therefore, three different sizes of graphene films are analysed.

[a]*Advanced Joining & Additive Manufacturing R&D Department, Korea Institute of Industrial Technology, Incheon 21999, Republic of Korea. E-mail: lty1002@kitech.re.kr; yoos@kitech.re.kr*

[b]*Department of Physics, Sungkyunkwan University, Suwon 16419, Republic of Korea*

[c]*Memory Division, Samsung Electronics, Hwaseong 18448, Republic of Korea. E-mail: jy1070.kim@samsung.com*

Experimental

Fig. 1 shows a schematic diagram of the synthesis procedure for the BTO powder particles encapsulated by rGO (hereafter rGO@BTO). The rGO@BTO was synthesized as follows. A mixture consisted of the BTO powder particles (US Research Nanomaterials, US3829, an average particle size of 300 nm) and hydrogen peroxide (H_2O_2) was stirred at 110 °C for 3 h. And then, 20 wt% H_2O_2-treated BTO powder particles were dispersed in 70 wt% *N*,*N*-dimethylformamide (DMF) solvent by sonication for 30 min. In order to obtain the NH_2-modified BTO powder, 10 wt% (3-aminopropyl)trimethoxysilane (APTMS, Sigma Aldrich) is added and then, stirred for 24 h.

Separately, the phenyl isocyanate-functionalized GO platelets (0.106 wt%) were dispersed in the deionized (D.I.) water by sonication. The size of the GO platelet was controlled by using the horn-type sonication, followed by the three different sonication times, *i.e.* 0, 30, and 60 min, respectively.

Next, the NH_2-modified BTO powders were added to the GO suspension for the encapsulation, and this mixture was stirred for 24 h, where the final loadings of the H_2O_2-treated BTO powder and GO platelets were 15.5 wt% and 0.1 wt%, respectively, in 84.1 wt% DMF/D.I. The solution is washed three times with D.I. water and (1,1)-dimethylhydrazine (reduction/deoxygenation agent) is added to the GO@BTO to complete the reduction process, as shown in Fig. 1.[28] The rGO@BTO powders were ready for dielectric films after washing with D.I. water.

Four series of films, with pure BTO and rGO@BTO powders with three different sizes of the rGO platelets were prepared. The fabrication process of the composite film was as follows: 16 wt% cyanoethyl pullulan (hereafter CEP, Shin-Etsu Chemical, the molecular weight of 438 000) was dissolved in 84 wt% DMF and then, stirred for 24 h. The rGO@BTO powders with the three different sized rGO, as well as the pure BTO powders, were dispersed in the CEP polymer by wet ball-milling (alumina balls with a diameter of 3 mm) to obtain homogeneous dispersion of the composite mixture. The final loading of the pure BTO and rGO@BTO powder was 40 wt% in 60 wt% CEP polymer solution.

All the dielectric solutions were spin-coated onto an ITO-glass at 1000 rpm and dried at 130 °C for 30 min (see Fig. 2a). Subsequently, a 500 nm-thick Al electrode is deposited by thermal evaporation. The thickness of all the dielectric composite films was maintained at approximately, 4 μm, as shown in Fig. 2b. The composite films are designated with the acronyms of REF0, RS00, RS30, and RS60, for pure BTO and BTO encapsulated by rGO with sonication times for 0, 30, and 60 min, respectively (see Fig. 1).

The morphology of the rGO@BTO powder was examined by scanning electron microscopy (SEM; JEOL, JSM7600F) and transmission electron microscopy (TEM; FEI, Tecnan G2 F20). The lattice vibrations in the powder were measured by Raman (WiTec Alpha, 300 micro-Raman imaging system; 532 nm excitation laser) and FT-IR (Bruker, Vertex 70) spectroscopy. The electrical and dielectric properties of the composite films were measured by a semiconductor device analyzer (Agilent, 4145B) which varies in frequency from 100 Hz to 10 kHz at 0.1 V. The thicknesses of the composite films were obtained using a Dektak 6M stylus surface profilometer.

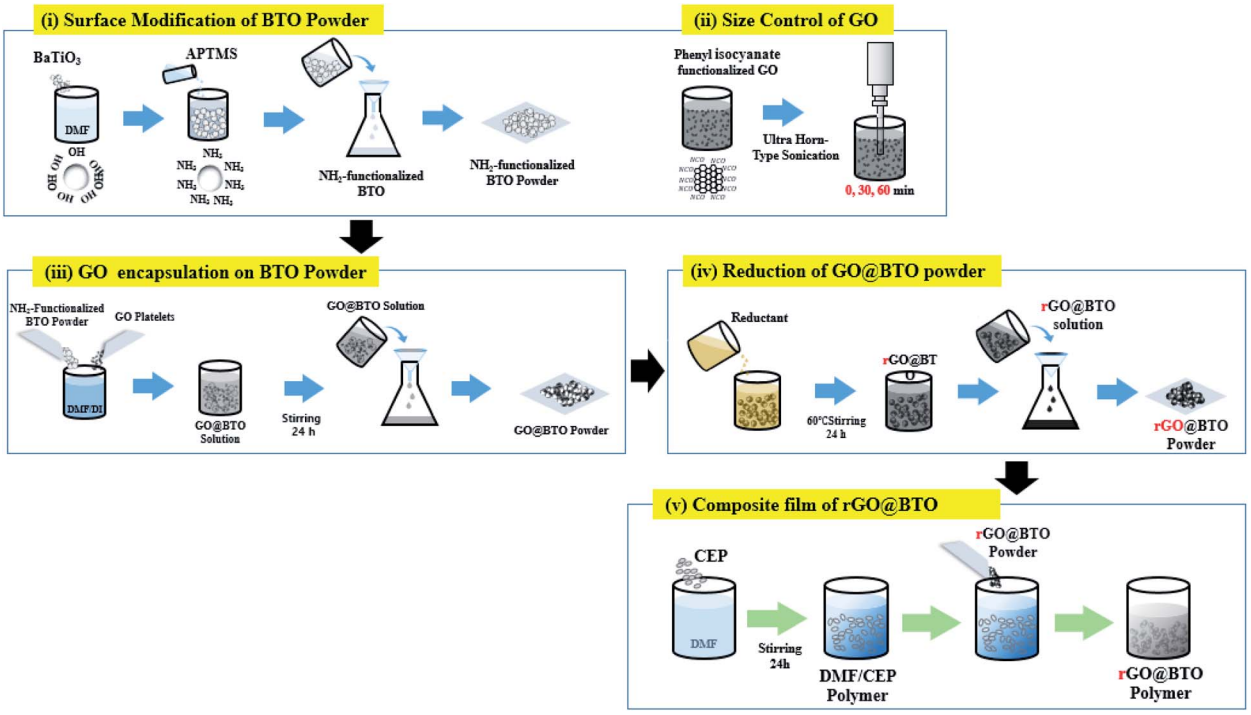

Fig. 1 Schematic diagram of synthesis process of rGO-encapsulated barium titanate (rGO@BTO), and the rGO@BTO/polymer dielectric composite.

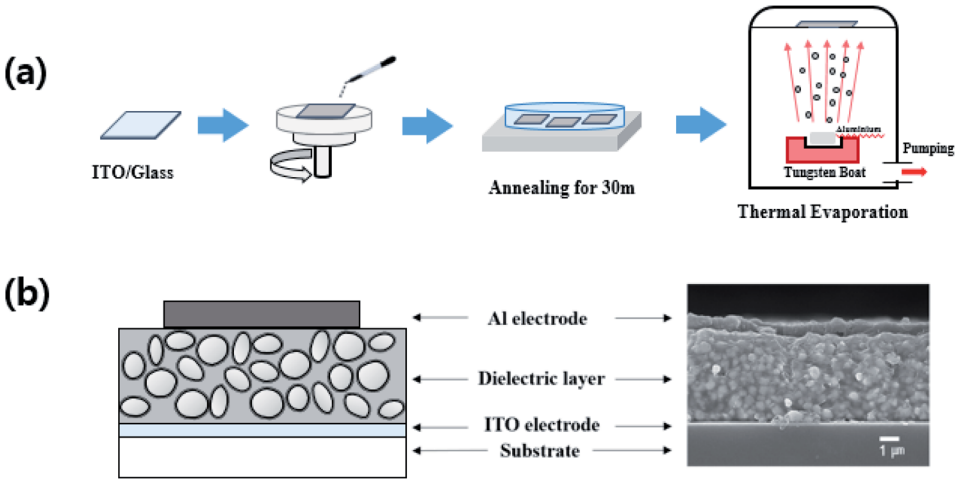

Fig. 2 Schematic diagram of synthesis process of (a) rGO-encapsulated barium titanate (rGO@BTO), and (b) the rGO@BTO/polymer dielectric composite.

Results and discussion

Fig. 3a exhibits the SEM images of the GO platelets obtained from the controlled size for sonication times, *i.e.*, 0, 30, and 60 min, respectively. It indicates that the size and thickness of the GO platelets decrease with the increase in the sonication time. The average diameter of RS00, RS30, and RS60 are 7, 1, and 0.6 μm, respectively. Particularly, RS60 presents a wide range of distribution for the GO platelets (see Fig. 3a), because the long-time ultra-sonication helps separate and decrease the thickness and size of the graphene platelets which are aggregated from each other. In general, the ultra-sonication has been utilized in the graphene exfoliation and/or flake dimension control. This fundamental mechanism can be interpreted through the inertial cavitation. During the sonication, graphene oxide platelets were fractured in a multiplicative process by the shockwaves. The mean platelet size of the graphene oxide would progressively decrease until the platelets are small enough. The shapes of the graphene oxide platelets could be square, elongated, or simply irregular.[30]

The morphology of the BTO powder particles before and after encapsulation by rGO is analysed by TEM, as shown in Fig. 3b. The encapsulation of the BTO powder particles by a thin layer of rGO can be easily confirmed by comparing two images. The thickness of the rGO is maintained at ~5 nm for RS60, as shown in Fig. 3b. Fig. 3c shows SEM images of rGO@BTO film with different thicknesses. It was difficult to characterize the morphology of rGO@BTO by SEM.

The Raman spectra are characterized under the pure BTO film and the rGO-encapsulated BTO films which results in three different sizes of rGO platelets based on the ultra-sonication time, as shown in Fig. 4. Typically, the BTO peaks of all the dielectric films are exhibited around 254 cm^{-1} [A1(TO)], 304 cm^{-1} [B1, E(TO + LO)], 513 cm^{-1} [A1, E(TO)], and 714 cm^{-1} [A1, E(LO)] (see Fig. 4).[31] However, the normalized intensities of the rGO@BTO films are decreased overall and also present broad and weak peaks when compared to the pure BTO film.[31]

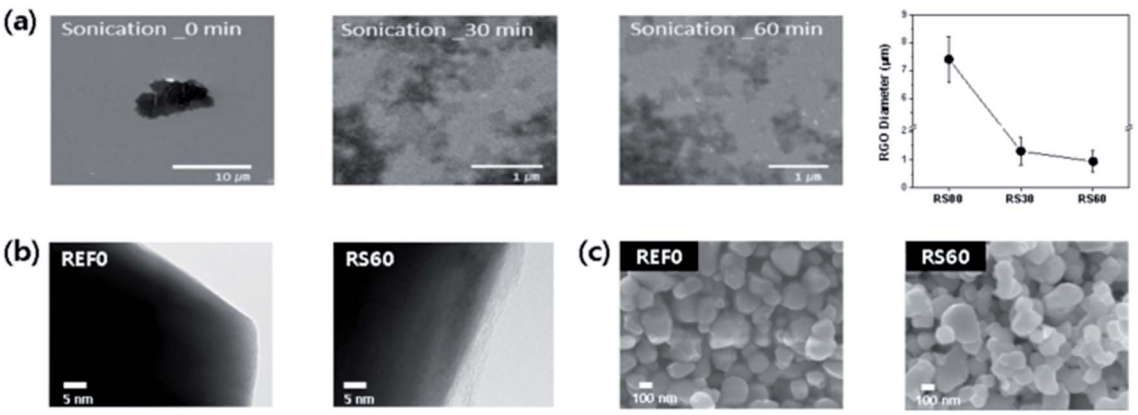

Fig. 3 (a) SEM images of three different sizes of GO platelets obtained by varying the sonication time, *i.e.*, 0, 30, and 60 min, respectively. (b) TEM images of the BTO powder particles before (REF0) and after rGO encapsulated BTO (RS60) and (c) SEM morphology of the BTO (REF0) and the rGO@BTO (RS60) films.

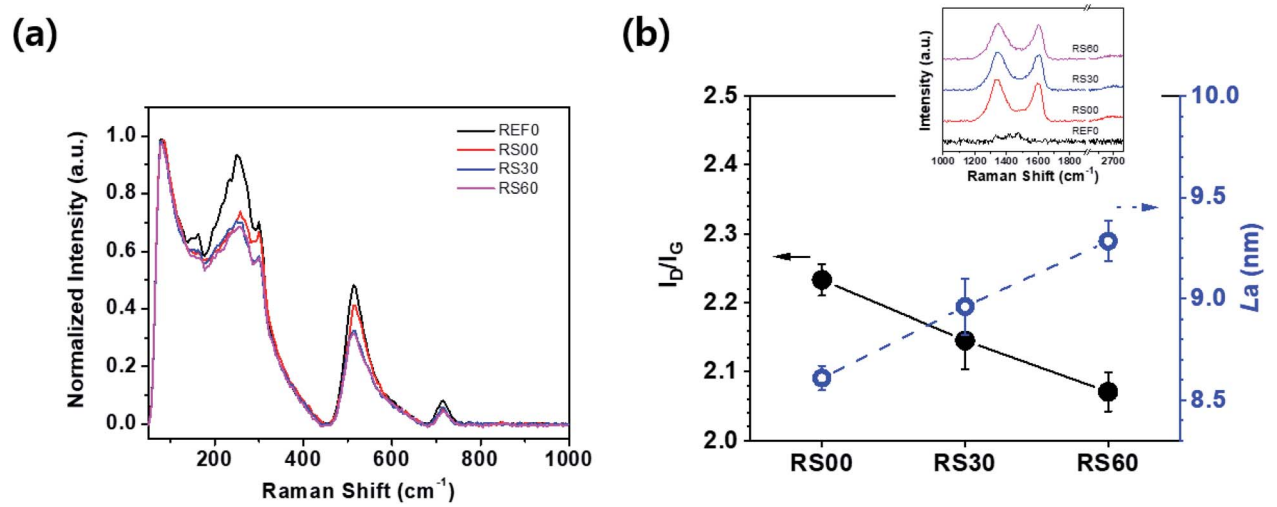

Fig. 4 Raman spectra of four dielectric films, *i.e.*, REF0, RS00, RS30, and RS60, respectively. (a) Raman spectra of the BTO peaks, and (b) the variation between I_D/I_G ratio and L_a corresponding to the sonication time. Inset is typical Raman spectra of rGO peaks.

This result indicates that the BTO powder particles can be sufficiently encapsulated by the rGO platelets.[28,32,33] Particularly, RS60 of the smallest rGO platelets, exhibits the lowest normalized intensity for BTO peaks when compared to the other films, as shown in Fig. 4a. Therefore, it slightly affects the vibrational behavior of the dielectric films based on the graphene size. Additionally, the typical Raman spectra of the graphene peaks exhibit a peak around ~1344 cm^{-1} (defects in the graphene structure related D band), a peak around 1603 cm^{-1} (the G band related to the sp^2 carbon network and the number of graphene layers), and a peak around 2670 cm^{-1} (the very weak 2D band originating from the overtone of the D band), respectively (inset in Fig. 4b).[34,35] Fig. 4b shows the intensity ratio of the I_D/I_G[36–39] corresponding to the defects in the graphene film on BTO particles. The ID/IG ratios of RS00, RS30, and RS60 exhibit 2.23, 2.14, and 2.07, respectively. The size of GO platelets without introducing a significant number of basal plan defect in the GO decreases with increase in the treatment time during the sonication. It might be the removal of sp^3 defects, vacancy defects, and edge defects in GO platelets during the sonication.[40] RS60 exhibits fewer defects than the other films even though the ratios (I_D/I_G) of graphene exhibit a small difference in the values. The L_a values are calculated by using the Tuinstra–Koenig relation to confirm the correlation between the crystallite size (L_a) and the ratio of I_D/I_G, as follows:[41]

$$L_a\ (\text{nm}) = (2.4 \times 10^{-10})\ \lambda^4\ (I_D/I_G)^{-1} \quad (1)$$

where λ and I_D/I_G denote the laser wavelength and intensity of the D- (G-) band, respectively. This indicates that the La values increase from 8.6 to 9.2, with the decrease in the I_D/I_G values, as shown in Fig. 4b. This is because the small size graphene platelets are sufficiently encapsulated in the BTO powder particles to reduce the defects.

In order to further investigate the lattice vibration in the rGO@BTO, FT-IR spectroscopy was examined, as shown in Fig. 5. The pure BTO powder had peaks near 3800 (lattice OH), 3650 (surface OH), 1650 (H–O–H), 1480 (CO_3^{2-}), 560 (O6 octahedra deformation), and 430 cm^{-1} (BTO fingerprint absorption), as shown in Fig. 5, which are all characteristic peaks of the BTO powder.[42] For the case of the rGO@BTO powder (RS60), different peaks were detected near 3750 (OH), 2980 (CH_2), 1630 (C=C), 1480 (CH_3), 1250 (C–O–C), 1060 (C–O/Si–O–Si), and 800 cm^{-1} (C–C),[43] which can be attributed to the rGO and APTMS. The peaks near 3750 (OH), 1628 (C=C), 1060 (Si–O–Si/C–O), and 800 cm^{-1} (C–C) are affected by the rGO, while the peaks near 2980 (CH_2) and 1060 cm^{-1} (Si–O–Si/C–O) are due to the APTMS coupling agent.[44] The peaks near 3230 and 3365 cm^{-1} were due to the presence of the hydrogen bonding between the N–H group and the carbonyl groups.[45,46] However, these peaks showed the broad band because of the strong OH groups of BTO powders. The peak for APTMS, at 552 or 794 cm^{-1} (SiO–H) was not considered, because two strong peaks

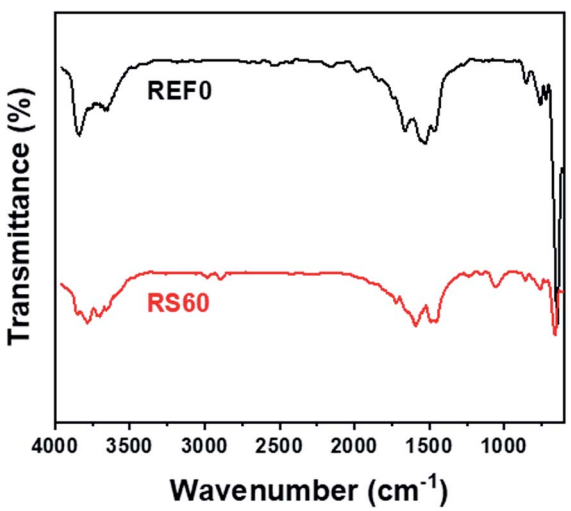

Fig. 5 FTIR spectra for two dielectric films of REF0 and RS60.

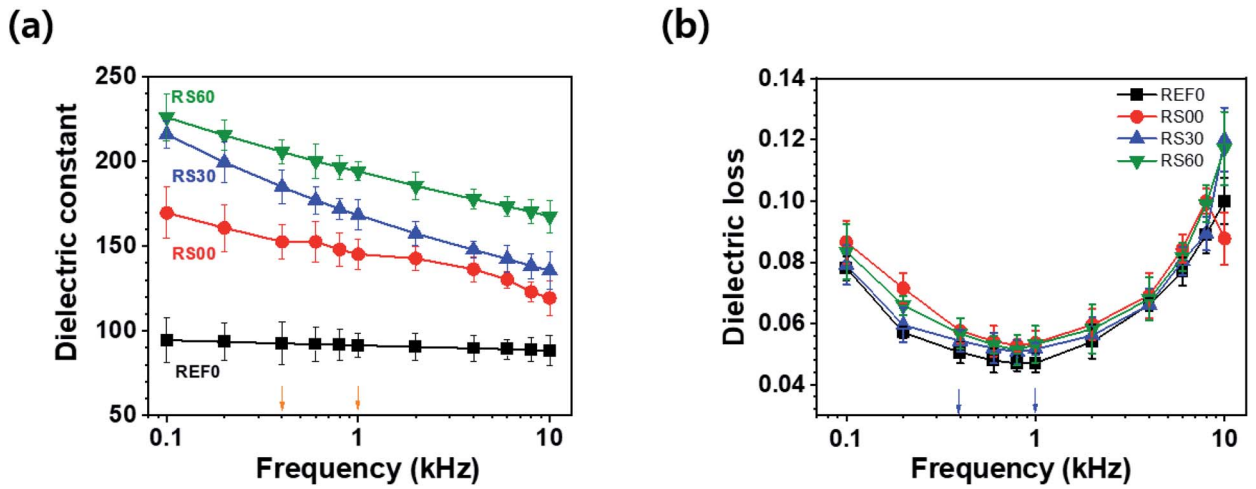

Fig. 6 (a) Dielectric constant and (b) dielectric loss corresponding to the applied frequencies from 0.1 to 10 kHz.

of the O6 octahedra deformation (560) and the BTO fingerprint absorption (430 cm^{-1}) were overlapped. As a result, TEM, Raman, and FT-IR spectroscopies indicate that the BTO powders were well encapsulated in the rGO platelets.

Fig. 6 depicts the frequency dependence of the dielectric constant and dielectric loss of all the films in the frequency range from 0.1 to 10 kHz. The dielectric constant of the pure BTO film, *i.e.*, REF0 in this case, remains almost unchanged, while the dielectric constant of the graphene-encapsulated BTO films decreases drastically with the increase in the frequency. All the graphene-encapsulated BTO films present 1.5 $\sim$ 2.5 times higher dielectric constant values and maintain low dielectric loss when compared to the pure BTO film (see Fig. 6). This frequency-dependence of the dielectric characteristics, *i.e.*, dielectric constant and loss, is attributed to the interfacial polarization, which is known as the Maxwell–Wagner–Sillars (MWS) polarization effect.[24,47,48] The dielectric constant of the rGO@BTO dielectric films decreases rapidly with increasing frequency up to 1 kHz, unlike the pure BTO film. This is because the MWS effect corresponds to the entrapment of the free charges between the insulator and conductor interfaces. Simultaneously, the numerous micro-capacitors which form between the graphene-encapsulated BTO and polymer can enhance the dielectric constant. Here, the best one is the RS60 case, due to the high dielectric constant and the low dielectric loss, as shown in Fig. 6.

The two frequencies for 0.4 and 1 kHz are selected to analyse the details of the dielectric characteristics, as shown in Fig. 7. At 0.4 kHz, the dielectric constants (losses) of the rGO@BTO films, *i.e.*, REF0, RS00, RS30, and RS60, exhibit values of 92.7 (0.051), 152.5 (0.058), 184.8 (0.054), and 205.5 (0.056), respectively. RS60 presents a 122% higher dielectric constant value and a mere 9% increase in the dielectric loss when compared to REF0 (see Fig. 7a). This result demonstrates that RS60 has a high dielectric constant along with a low dielectric loss. Such a factor can improve dielectric-based capacitor applications. Additionally, RS60 presents a 111% higher dielectric constant (from 92 to 194) and a mere 13% increase in the dielectric loss (from 0.047 to 0.053) when compared to REF0 at 1 kHz (see Fig. 7b). This implies that this result is obtained due to the existence of

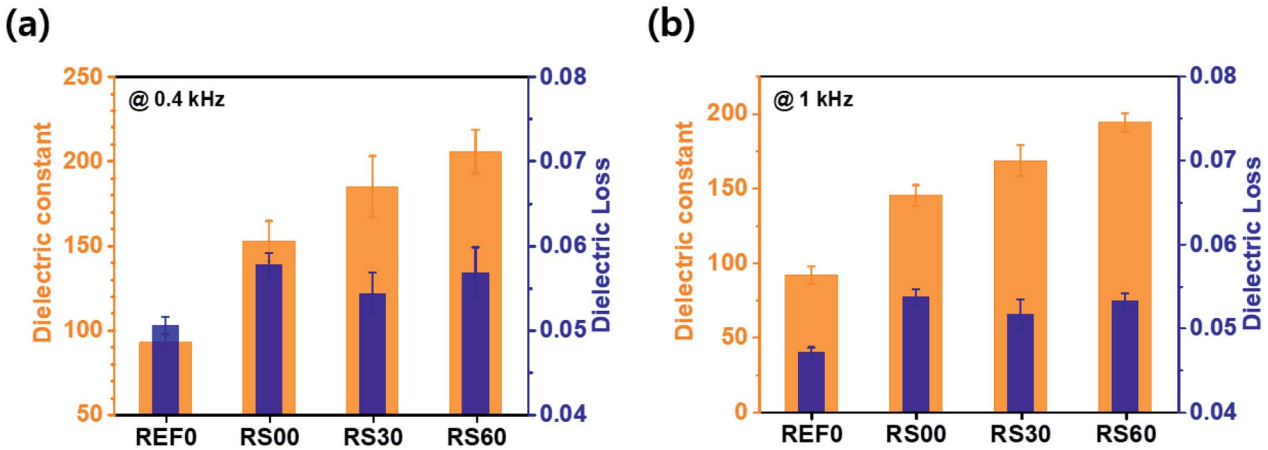

Fig. 7 Dielectric constants and dielectric losses at (a) 0.4 kHz and (b) 1 kHz.

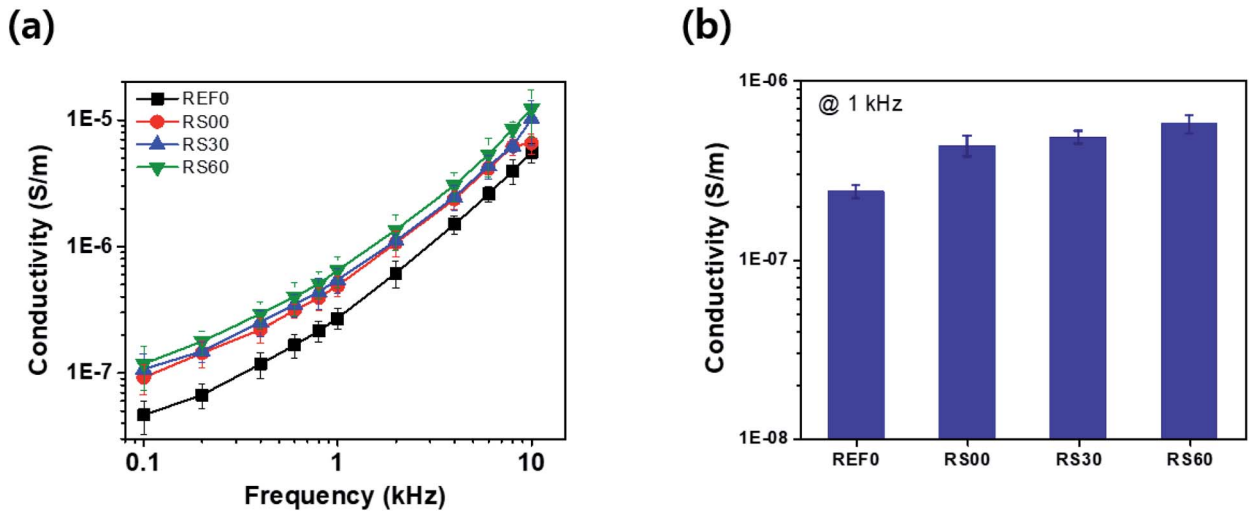

Fig. 8 (a) Conductivity corresponding to the applied frequency from 0.1 to 10 kHz at a fixed voltage of 0.1 V, and (b) 1 kHz.

graphene *via* the interface polarization and micro-capacitor effects.[28] The enhancement in the dielectric constant of the composite with RS60 is attributed to the interfacial polarization between the adjacent rGO@BTO particles and the numerous micro-capacitor effects produced by space charge polarization, following rGO platelets as micro-electrode and BTO as a dielectric medium.[28] The rGO platelets with controlled size, along with the virtual removal of the free rGO platelets during the encapsulation process, can reduce the percolative connection of the rGO platelets. Therefore, the rGO platelets with controlled size can reduce the percolation paths of graphene interconnections, by preventing the increasing conductivity. It can result in a higher dielectric constant and low dielectric loss in the dielectric film.

Fig. 8 depicts the dependence of the alternating current (AC) conductivity as a function of the frequency of the pure BTO film and the graphene-encapsulated BTO films to provide a better understanding of the electrical properties. All the rGO@BTO films have a slightly higher electrical conductivity when compared to the pure BTO film (see Fig. 8a). This can be attributed to the generation of the conductive graphene pathways. However, in this case, the AC conductivity of rGO@BTO is enhanced at a low rate due to its relatively low electrical conductivity by controlling the size of the rGO platelets. At 1 kHz, the electrical conductivity of the pure BTO film is 2.7×10^{-6} S m^{-1} and that with RS60 is 6.4×10^{-6} S m^{-1}, as shown in Fig. 8a. The dielectric loss and electrical conductivity values of all the rGO@BTO films are slightly increased when compared to the pure BTO film (see Fig. 8b). At the higher conductivity of the rGO platelets, the density of the accumulated charge carriers at the interfaces between the rGO platelets and the polymer would be increased, leading to an increased interfacial polarization that would contribute to an increased dielectric constant.[49]

Conclusion

This paper reports the successful fabrication of the dielectric film with rGO-encapsulated BTO by using the horn-type ultrasonication. The electrical conductivity, dielectric constant, and dielectric loss are effectively analysed by controlling the size of the graphene platelets. Especially, the dielectric constant of RS60, with the smallest size of graphene platelets, was 194 with a dielectric loss of 0.053 at a frequency of 1 kHz, while that with REF0, without graphene platelets, was 92 with a dielectric loss of 0.047. This implies that the significant increase in the dielectric constant with the low dielectric loss can be attributed to interfacial polarization and micro-capacitor effects due to the encapsulation between the adjacent small size of the rGO platelets and BTO powder particles. Therefore, the controlled size of the graphene platelets plays an important role in the enhancement of the dielectric properties. Considering the high dielectric performance, as well as the simplicity of the fabrication process, this film is promising for applications in charge-storage capacitors and antistatic materials.

Conflicts of interest

There are no conflicts to declare.

References

1 M. D. Stoller, S. J Park, Y. W. Zhu, J. H. An and R. S. Ruoff, *Nano Lett.*, 2008, **8**, 3498–3502.
2 X. J. Zhu, Y. W. Zhu, S. Murali, M. D. Stollers and R. S. Ruoff, *ACS Nano*, 2011, **5**, 3333–3338.
3 L. Wang, J. Lian, P. Cui, Y. Xu, S. Seo, J. Lee, Y. T. Chan and H. Lee, *Chem. Commun.*, 2012, **48**, 4052–4054.
4 D. P. Suhas, T. M. Aminabhavi, H. M. Jeong and A. V. Raghu, *RSC Adv.*, 2015, **5**, 100984–100995.
5 D. P. Suhas, A. V. Raghu, H. M. Jeong and T. M. Aminabhavi, *RSC Adv.*, 2013, **3**, 17120–17130.
6 T. Mathew, R. A. Sree, S. Aishwarya, K. Kounaina, A. G. Patil, P. Satapathy, S. P. Hudeda, S. S. More, K. Muthucheliyan, T. N. Kumar, A. V. Raghu, K. R. Reddy and F. Zameer, *FlatChem*, 2020, **23**, 100184.

7 S. Kumar, K. R. Reddy, C. V. Reddy, N. P. shetti, V. S. Sadhu, M. V. shankar, V. G. Reddy, A. V. Raghu and T. M. Aminabhavi, *Nanostructured materials for Environment applications*, 2021, pp. 485–519.
8 D. A. Nguyen, A. V. Raghu, J. T. Choi and H. M. Han, *Polym. Polym. Compos.*, 2010, **18**, 351–358.
9 H. B. Lee, A. V. Raghu, K. S. Yoon and H. M. Jeong, *J. Macromol. Sci., Part B: Phys.*, 2010, **40**, 802–809.
10 M. Tian, Z. Wei, X. Zan, L. Zhang, J. Zhang, Q. Ma, N. Ning and T. Nishi, *Compos. Sci. Technol.*, 2014, **99**, 37–44.
11 D. Wang, T. Zhou, J.-W. Zha, J. Zhao, C.-Y. Shi and Z.-M. Dang, *J. Mater. Chem. A*, 2013, **1**, 6162–6168.
12 K. Yang, X. Huang, L. Fang, J. He and P. Jiang, *Nanoscale*, 2014, **6**, 14740–14753.
13 W. Xu, Y. Ding, S. Jiang, L. Chen, X. Liao and H. Hou, *Mater. Lett.*, 2014, **135**, 158–161.
14 A. Ameli, M. Nofar, C. B. Park, P. Potshke and G. Rizvi, *Carbon*, 2014, **71**, 206–217.
15 M. Tian, Z. Wei, X. Zan, L. Zhang, J. Zhang, Q. Ma, N. Ning and T. Nishi, *Compos. Sci. Technol.*, 2014, **99**, 37–44.
16 C. Behera, P. Patel, N. Pradhan and R. N. P. Choudhary, *J. Mater. Sci.: Mater. Electron.*, 2022, **33**, 1657–1669.
17 E. Jiménez-Marín, J. Moreno-Valenzuela, M. Trejo-Valdez, A. Martinez-Rivas, J. R. Vargas-García and C. Torres-Torres, *Opt. Express*, 2019, **27**, 7330–7343.
18 B. Jiang, J. Iocozzia, L. Zhao, H. Zhang, Y. W. Harn, Y. Chen and Z. Lim, *Chem. Soc. Rev.*, 2019, **48**, 1194–1228.
19 B. Jiang, X. Pang, B. Li and Z. Lin, *J. Am. Chem. Soc.*, 2015, **137**, 11760–11767.
20 J. Yin, Y. Shui, Y. Dong and X. Zhao, *Nanotechnol*, 2014, **25**, 045702.
21 M. J. Bae, J.-Y. Kim, S. H. Park, T. Jeong, S. Song, J. Lee, I. Han, D. Jung, J. B. Yoo, C. Liu and S. Yu, *Electron. Lett.*, 2011, **47**, 664–665.
22 S.-Y. Jun, H. Lim, D. Jung, J. H. Ko, M. J. Seong, J. Y. Kim and S. Yu, *Carbon*, 2019, **146**, 462–467.
23 Y.-J. Wan, P.-L. Zhu, S.-H. Yu, W.-H. Yang, R. Sun, C.-P. Wong and W.-H. Liao, *Compos. Sci. Technol.*, 2017, **141**, 48–55.
24 M. Yang, H. Zhao, C. Hu, P. Haghi-Ashtiani, D. He, Z.-M. Dang and J. Bai, *Phys. Chem. Chem. Phys.*, 2018, **20**, 2777–2786.
25 I. Singh, P. K. Bhatnagar, P. C. Mathur, I. Kaur, L. M. Haradwaj and R. Pandey, *Carbon*, 2008, **46**, 1141–1144.
26 C. Pecharromán and J. S. Moya, *Adv. Mater.*, 2000, **12**, 294–297.
27 S. Kirkpatr, *Rev. Mod. Phys.*, 1973, **45**, 574–588.
28 S.-Y. Jun, D. Jung, J.-Y. Kim and S. Yu, *Mater. Chem. Phys.*, 2020, **255**, 123533.
29 Z. T. Luo, Y. Lu, L. A. Somers and A. T. Johnson, *J. Am. Chem. Soc.*, 2009, **131**, 898–899.
30 A. Liscio, K. Kouroupis-Agalou, X. D. Betriu, A. Kovtun, E. Treossi, N. M. Pugno, G. D. Luca, L. Giorgini and V. Palermo, *2D Mater.*, 2017, **4**, 025017.
31 S. Fuentes, R. A. Zarate, E. Chavez, P. Munoz, M. Ayala, R. Espinoza-Gonzalez and P. Leyton, *J. Alloys Compd.*, 2010, **505**, 568–572.
32 Z. Sun, X.-L. Wu, J. Xu, D. Qu, B. Zhao, Z. Gu, W. Li, H. Liang, L. Gao, Y. Fan, K. Zhou, D. Han, S. Gan, Y. Zhang and L. Niu, *Small*, 2020, **16**, 1907670.
33 J. H. Shim, Y. M. Kim, M. Park, J. Kim and S. Lee, *ACS Appl. Mater. Interfaces*, 2017, **9**, 18720–18729.
34 X. Han, S. Chen, X. Lv, H. Luo, D. Zhang and C. R. Bowen, *Phys. Chem. Chem. Phys.*, 2018, **20**, 2826–2837.
35 S.-G. Kim, O.-K. Park, J. H. Lee and B.-C. Ku, *Carbon Lett.*, 2013, **14**, 247–250.
36 R. Genc, M. O. Alas, E. Harputlu, S. Repp, N. Kremer, M. Castellano, S. G. Colak, K. Ocakoglu and E. Erdem, *Sci. Rep.*, 2017, **7**, 11222.
37 M. Buldu-Akturk, M. Toufani, A. Tufanic and E. Erdem, *Nanoscale*, 2022, **14**, 3269–3278.
38 C. V. Pham, S. Repp, R. Thomann, M. Krueger, S. Weber and E. Erdem, *Nanoscale*, 2016, **8**, 9682–9687.
39 S. Repp, E. Harputlu, S. Gurgen, M. Castellano, N. Kremer, N. Pompe, J. Wörner, A. Hoffmann, R. Thomann, F. M. Emen, S. Weber, K. Ocakoglu and E. Erdem, *Nanoscale*, 2018, **10**, 1877–1884.
40 A. Eckmann, A. Felten, A. Mishchenko, L. Britnell, R. Krupke, K. S. Novoselov and C. Casiraghi, *Nano Lett.*, 2012, **12**, 3925–3930.
41 F. Tuinstra and J. L. Koenig, *J. Compos. Mater.*, 1970, **4**, 492–499.
42 M. C. B. Lopez, G. Fourlaris, B. Rand and F. L. Riley, *J. Am. Ceram. Soc.*, 1999, **82**, 1777–1786.
43 L. Xie, X. Huang, Y. Huang, K. Yang and P. Jiang, *ACS Appl. Mater. Interfaces*, 2013, **5**, 1747–1756.
44 S. Yang, X. Feng, S. Ivanovici and K. Mullen, *Angew. Chem., Int. Ed.*, 2010, **49**, 8408–8411.
45 A. V. Raghu and H. M. Jeong, *J. Appl. Polym. Sci.*, 2008, **107**, 3401–3407.
46 A. V. Raghu, H. M. Jeong, J. H. Kim, Y. R. Lee and Y. B. Cho, *Macromol. Res.*, 2008, **16**, 194–199.
47 C.-W. Nan, Y. Shen and J. Ma, *Annu. Rev. Mater. Res.*, 2010, **40**, 131–151.
48 M. Rahimabady, M. S. Mirshekarloo, K. Yao and L. Lu, *Phys. Chem. Chem. Phys.*, 2013, **15**, 16242.
49 Z.-M. Dang, Y.-H. Zhang and S.-C. Tjong, *Synth. Met.*, 2004, **146**, 79–84.